Journal of Sound and Vibration 642 (2026) 119953

Contents lists available at ScienceDirect

Journal of Sound and Vibration

journal homepage: www.elsevier.com/locate/jsvi

A boundary-field integral formulation for nonlinear scattering of acoustic waves by deforming bodies

B. De Rubeis, M. Gennaretti *, C. Poggi, G. Bernardini

Department of Civil, Computer Science and Aeronautical Technologies Engineering, Roma Tre University, Via Volterra 62, Rome, 00146, Italy

ARTICLE INFO

Keywords:
Nonlinear sound scattering
Deforming scatterer
Deformable-boundary integral formulation
Harmonic-nonlinear boundary element method

ABSTRACT

Sound scattering by deforming bodies is investigated through a novel nonlinear boundary-field integral formulation based on the velocity potential equation. The proposed approach applies an iterative cascade solution strategy to account for nonlinearities due to irrotational flow field generated by moving boundaries. The resulting formulation is solved numerically through a boundary element method combined with the harmonic-balance technique to capture the multi-chromatic scattered signal. The numerical investigation studies the sound scattered by a pulsating sphere impinged by a plane wave. It shows that the proposed iterative solution algorithm is able of providing convergent nonlinear scattered solution in a few iterations. The results demonstrate that fluid nonlinearities associated with the amplitudes of the sphere pulsation and the incident wave significantly affect the directivity pattern of the scattered signal.

1. Introduction

The emergence of novel aircraft architectures conceived for next-generation aeronautical operations has opened promising opportunities to enhance mobility and support new mission profiles. The feasibility of these innovative concepts, however, is strongly conditioned by their environmental impact, with particular emphasis on chemical emissions and noise generation [1].

Addressing these issues requires the integration of acoustic analyses from the earliest phases of the design process. Incorporating such evaluations at the conceptual and preliminary levels is essential for limiting noise exposure and for ensuring compliance with the stringent quantitative objectives established by international regulatory bodies [2] and by the Flightpath 2050 strategic vision [3]. These increasingly demanding targets motivate the development and adoption of robust and computationally efficient prediction methodologies.

Compared with conventional aircraft, the acoustic behaviour of these emerging configurations is influenced by a wider range of physical mechanisms. Key factors include the aerodynamic interactions arising in configurations with distributed propulsion and the aeroacoustic and aerodynamic effects produced by structural deformations in highly flexible airframes [4,5]. These complexities highlight the need for accurate modelling strategies capable of capturing the coupled flow-structure-acoustic dynamics inherent in such systems.

Furthermore, the vehicle's airframe itself drastically alters the noise radiated by the propulsion system. Understanding these installation effects is a primary concern, typically modeled using scattering formulations. These methods assume that the incident pressure wave is uncoupled from the scatterer's surface, allowing the acoustic field to be split into incident and scattered components. This decoupling enables independent evaluations: the incident field is first calculated assuming an isolated, "frozen" source, while

* Corresponding author.
E-mail address: m.gennaretti@uniroma3.it (M. Gennaretti).

https://doi.org/10.1016/j.jsv.2026.119953
Received 29 August 2025; Received in revised form 6 June 2026; Accepted 8 June 2026
Available online 10 June 2026

Nomenclature

a_d	amplitude of sphere pulsations
A^I	amplitude of incident velocity potential plane wave
$\mathbf{a}_1,\ \mathbf{a}_2,\ \mathbf{a}_3$	covariant basis vectors
A_{km}, B_{km}, C_{km}	BEM surface coefficients
BEM	Boundary Element Method
$\mathbf{D}, \mathbf{D}_f, \mathbf{D}^{nc(s)}_{mc(s)}$	matrices of harmonic-BEM coefficients
$c,\ c_0$	local and undisturbed speed of sound
d	distance of observers from sphere center
$\mathbf{f}, \mathbf{f}_f, \mathbf{f}^{\eta}_{nc(s)}, \mathbf{f}^{\sigma}_{nc(s)}$	vectors of harmonic-BEM forcing terms
G_0	spatial term of Green's function
$\boldsymbol{J}$	Jacobian of curvilinear coordinate transformation
H_{kh}	BEM volume coefficients
k_d	deformation wave number, ω_d/c_0
k_I	wave number of incident potential
$\mathbf{M}$	Mach number of scatterer surface points
M_n	Mach number in normal direction, $\mathbf{n}$
$\mathbf{n}$	outward unit normal vector of boundary surface
N_a	number of harmonics
N_c	number of parallel circles
N_m	number of meridians
N_o	number of observers
N_p	number of surface discretization panels
N_r	number of radial volume elements
N_S	number of significant scattered potential components
N_v	number of discretization volume elements
r	distance between emitting and receiving points
r_0	radius of undeformed sphere
$\mathcal{S}$	body surface of scatterer
S^I_i	intensities of external frozen sources
$\mathbf{u}, u$	fluid velocity vector and magnitude
$\mathbf{v}_\xi$	velocity of scatterer surface points
$\mathcal{V}_\Omega$	volume mapping in (ξ^1, ξ^2, ξ^3)-domain
$\mathbf{x}$, $\mathbf{x}_*$	emitting and receiving point positions
θ	signal propagation delay
σ	non-linear terms of the velocity potential equation
σ^{EXT}	external forcing terms of velocity potential equation
φ	total velocity potential
$\boldsymbol{\varphi}$	vector of harmonic-BEM velocity potential
φ^0	velocity potential radiated by scatterer motion
φ^I, φ^S	incident and scattered velocity potential
$\varphi^{S,j}$	jth cascade component of φ^S
η	normal derivative of the velocity potential
η^0	normal derivative of φ^0
η^j	normal derivative of $\varphi^{S,j}$
Ω	boundary surface mapping in (ξ^1, ξ^2)-plane
ω	fundamental angular frequency of Fourier series
ω_d	angular frequency of sphere pulsations
ω_I	angular frequency of impinging wave

the remaining vehicle components act solely as scatterers. This avoids the severe computational burden of solving the source and scatterer simultaneously.

Extensive literature has addressed this topic, primarily modeling the airframe as a rigid stationary or moving object (e.g., Refs. [6–10]). Many of these models rely on velocity potential or acoustic pressure formulations derived from the Lighthill [11] or Ffowcs Williams and Hawkings (FW-H) [12] equations (see, for instance, Refs. [13,14]). Notably, linear boundary integral formulations for the FW-H equation and those for velocity potential perturbations yield distinct scattering predictions for moving bodies. This discrepancy arises because neglecting nonlinear field terms affects the two formulations differently in the presence of a non-uniform meanflow [14].

Beyond rigid bodies, the problem of sound scattered by deforming surfaces has also been explored. Using a perturbation method applied to the linear wave equation, Censor [15,16] introduced analytical solutions for simple geometries like cylinders and spheres. He demonstrated that kinematic nonlinearities in the boundary conditions generate a multi-harmonic spectrum, which depends on both the scatterer's motion and the chosen perturbation order.

Alternatively, multiple tones can be generated by fluid nonlinearities arising from the flow induced by the scatterer's dynamic deformations. This phenomenon was analyzed by Piquette [17] for a 2D infinitely long, radially vibrating cylinder interacting with a plane wave, under the assumption of a rigid scatterer where nonlinearities emerge from combining incident, radiated, and scattered waves. To weigh the relative impact of these two multi-harmonic sources, Mujica et al. [18] experimentally investigated waves scattered by a vibrating piston. They successfully identified two distinct scattering regimes: one dominated by the boundary conditions on the vibrating surface, and another driven primarily by fluid nonlinearities.

In this framework, this paper considers the analysis to an arbitrarily shaped three-dimensional body impinged by an incident wave. To this aim, it introduces a novel velocity-potential solution approach for nonlinear sound scattering.

The scattered velocity-potential field is obtained through application of a deformable-boundary integral formulation derived as a specific case of the integral solution of the arbitrarily forced wave equation recently developed by the authors [19,20]. Building upon the study presented in [21], which introduced a linear boundary-integral approach for sound scattering capable of capturing multi-harmonic effects induced by boundary conditions on strongly deforming surfaces, the present work provides a significant methodological extension. In particular, the formulation proposed here includes, for the first time within this framework, the contribution of the nonlinear field terms that arise from the flow generated by the scatterer's deformation and that act as sources in the forced wave equation. This advancement enables a more complete and physically consistent prediction of the scattered field for configurations involving large, dynamically evolving structural motions.

The scattered sound is described through a technique consisting of the superposition of incremental velocity potential solutions (here called velocity potential cascade solution) combined with a harmonic-balance technique. Specifically, the incremental velocity potential solutions are forced by progressively decreasing fluid nonlinearities given by the combination of incident and scattered signals with the velocity potential related to the flow-field generated by the motion of the scatterer. These incremental velocity potentials are determined through the application of the deformable-boundary integral formulation introduced in [19,20].

The description of the velocity potential cascade solution is given in Section 2, while the boundary-element-method/harmonic-balance numerical algorithm applied to determine the solution of the deformable-boundary integral formulation is outlined in Section 3. The results of a numerical investigation are discussed in Section 4. The analyses concern the sound scattered by a pulsating sphere impinged by a plane acoustic waves, considering sphere motions for which the nonlinear terms associated with the radiated sound are negligible, so as to focus on nonlinear scattering effects. The numerical investigation examines the convergence rate of the proposed nonlinear solution algorithm and the effects of the fluid flow generated by the surface pulsations on the scattered signal. The influence of the amplitude of the incident signal on the directivity pattern of the scattered sound is also investigated.

2. Nonlinear integral formulation for sound scattered by deforming bodies

Let us consider a body moving in a perfect, inviscid gas, initially at rest, and a frame of reference, $\mathcal{R}(\mathbf{x})$, fixed with the far-field undisturbed fluid (referred to as FFR). Then, let us express the generated irrotational flow field velocity, $\mathbf{u}$, with respect to FFR through the velocity potential φ such that $\mathbf{u} = \nabla\varphi$. Combining the mass conservation equation with Bernoulli's theorem for isentropic flows, the following inhomogeneous wave equation governing the velocity potential is obtained

$$-\Box^2\varphi = \nabla^2\varphi - \frac{1}{c_0^2}\frac{\partial^2\varphi}{\partial t^2} = \sigma + \sigma^{\mathrm{EXT}} \tag{1}$$

where $\Box^2$ represents the d'Alembert operator, c_0 is the speed of sound of the undisturbed fluid, σ is the nonlinear forcing term that is given by

$$\sigma = \frac{1}{c_0^2}\left[(c_0^2 - c^2)\nabla^2\varphi + 2\nabla\varphi\cdot\nabla\dot{\varphi} + \frac{1}{2}\nabla\varphi\cdot\nabla(u^2)\right] \tag{2}$$

with c denoting the local speed of sound, while $\dot{(\cdot)} = \partial/\partial t$. In addition, σ^{EXT} takes into account the effects deriving from the possible presence of external forcing sources independent of the body motion.

The differential problem is completed by the boundary condition of perturbation potential vanishing infinitely far from the moving body ($\varphi \to 0$ as $\mathbf{x} \to \infty$, Dirichlet type) and the imposition of impermeability of the body surface (Neumann type)

$$\eta = \frac{\partial\varphi}{\partial n} = \mathbf{v}_\xi \cdot \mathbf{n}, \qquad \mathbf{x} \in S \tag{3}$$

where $\mathbf{n}$ is the unit vector normal to the surface S of the scattering body, and $\mathbf{v}_\xi$ represents the velocity of its points.

As demonstrated and discussed in [19,20] (to which the reader is referred for details), the solution of Eq. (1) for the velocity potential around moving and deforming bodies is obtained by the application of the boundary integral equation method, which is based on the introduction of the free-space Green's function. This function, G, is defined as the fundamental solution of the wave equation, namely, the solution of the following wave equation forced by time and space impulses

$$\nabla^2 G - \frac{1}{c_0^2}\frac{\partial^2 G}{\partial t^2} = \delta(\mathbf{x} - \mathbf{x}_*)\,\delta(t - t_*) \tag{4}$$

associated with the boundary condition $G = 0$ for $|\mathbf{x} - \mathbf{x}_*| \to \infty$, and the time conditions $G = \dot{G} = 0$ for $t \to \infty$, and reads [22]

$$G(\mathbf{x} - \mathbf{x}_*, t - t_*) = \frac{-1}{4\pi r}\,\delta\left(t - t_* + \frac{r}{c_0}\right) \tag{5}$$

where $r = |\mathbf{r}| = |\mathbf{x}_* - \mathbf{x}|$.

The next steps of the method consist of: (i) recasting the problem in Eq. (1) into an equivalent infinite-space one by extending the velocity potential to the entire $\mathbb{R}^3$ domain as $\bar{\varphi} = \varphi\, H(f)$, where H represents the Heaviside function and the function $f = f(\mathbf{x}, t)$ is such that $f = 0$ if $\mathbf{x} \in \mathcal{S}$, $f > 0$ if $\mathbf{x}$ is outside the body, $f < 0$ if $\mathbf{x}$ is inside the body; this yields

$$\nabla^2\bar{\varphi} - \frac{1}{c_0^2}\frac{\partial^2\bar{\varphi}}{\partial t^2} = H\sigma + \nabla H\cdot\nabla\varphi + \nabla\cdot(\varphi\nabla H) - \frac{1}{c_0^2}\left[\frac{\partial H}{\partial t}\frac{\partial\varphi}{\partial t} + \frac{\partial}{\partial t}\left(\varphi\frac{\partial H}{\partial t}\right)\right] \tag{6}$$

(ii) combining the multiplication of function G with Eq. (6) with Eq. (4) multiplied by the function $\bar{\varphi}$; (iii) integrating over the entire $\mathbb{R}^3$ domain and over time by exploiting the generalized time and space functions.

For $\mathbf{x}_*$ and t_* representing, respectively, external position and time of observation, this yields the following boundary integral solution

$$\begin{aligned}\varphi(\mathbf{x}_*, t_*) = &\iint_\Omega \left[(1 - M_n^2)\frac{\partial\varphi}{\partial n}G_0\right]J\Big|_\theta \mathrm{d}\xi^1\mathrm{d}\xi^2 - \iint_\Omega \left[M_n\mathbf{M}\cdot\nabla_t\,\varphi\, G_0\right]J\Big|_\theta \mathrm{d}\xi^1\mathrm{d}\xi^2\\ &- \iint_\Omega \left[\varphi\frac{\partial G_0}{\partial n} - \frac{\partial\varphi}{\partial t}\Big|_\xi\frac{M_n}{c_0}G_0\right]J\Big|_\theta \mathrm{d}\xi^1\mathrm{d}\xi^2 - \iint_\Omega \frac{1}{\Theta}\frac{\partial}{\partial t}\Big|_\xi\left[\varphi\, G_0\, J\left(\frac{\mathbf{e}_r\cdot\mathbf{n}}{c_0} - \frac{M_n}{c_0}\right)\right]\Big|_\theta \mathrm{d}\xi^1\mathrm{d}\xi^2\\ &+ \iiint_{\mathcal{V}_\Omega}\sigma\, G_0\, J\Big|_\theta \mathrm{d}\xi^1\mathrm{d}\xi^2\mathrm{d}\xi^3\end{aligned} \tag{7}$$

which corresponds to Eq. (27) of Ref [19]., once the correction given in [20] is considered and the symbols $\Psi, k_1, k_2, \mathbf{z}, \mathbf{Z}$, $\mathbf{w}$, χ, there introduced to express the arbitrarily-forced acoustic wave equation, are defined as $\Psi = \varphi$, $\mathbf{z} = \nabla\varphi$, $\mathbf{Z} = \varphi\mathbf{I}$, $k_1 = -1/c_0^2\,(\partial\varphi/\partial t)$, $k_2 = -\varphi/c_0^2$, $\mathbf{w} = \mathbf{0}$, $\chi = H\sigma$, with $\mathbf{I}$ denoting the identity tensor. In the above equation, (ξ^1, ξ^2, ξ^3) is a system of curvilinear coordinates defined over the body surface and the region around it, with the points of the body surface identified as those for which $\xi^3 = 0$. The symbols Ω and $\mathcal{V}_\Omega$ denote, respectively, the domains in the (ξ^1, ξ^2)-space and in the (ξ^1, ξ^2, ξ^3)-space onto which the body surface and the adjacent fluid region are mapped. In addition, $G_0 = -1/(4\pi r)$, $\mathbf{M} = \mathbf{v}_\xi/c_0$, $M_n = \mathbf{M}\cdot\mathbf{n}$, $\mathbf{e}_r = \mathbf{r}/r$, $J = |\mathbf{a}_1\times\mathbf{a}_2\cdot\mathbf{a}_3|/|\Theta|$ is the Jacobian of the curvilinear coordinate transformation ($\mathbf{a}_k$ are the covariant base vectors related to (ξ^1, ξ^2, ξ^3)) with $\Theta = (1 - \mathbf{M}\cdot\mathbf{e}_r)$. Furthermore, the symbol $(\ldots)|_\theta$ indicates that the integrands must be evaluated at time $t = t_* - \theta$, which is the instant at which the surface of the body emitted the signal that at time t_* reaches the observer. Finally, note that the integral formulation in Eq. (7) is obtained by expressing the gradient operator as $\nabla\varphi = \nabla_t\,\varphi + (\partial\varphi/\partial n)\,\mathbf{n}$ and noting that the time derivative at FFR fixed points is recast as

$$\frac{\partial\varphi}{\partial t} = \frac{\partial\varphi}{\partial t}\Big|_\xi - \mathbf{v}_\xi\cdot\nabla\varphi$$

2.1. Cascade solution approach for nonlinear velocity potential scattering

When the boundary integral formulation in Eq. (7) is applied to problems for which the nonlinear field term is not negligible, the numerical evaluation of the velocity potential over the body surface and its neighborhood requires the adoption of an iterative solution scheme. This is the case examined in this work, whose objective is the prediction of sound scattering in the presence of fluid nonlinearities due to dynamic deformation of the scatterer. Therefore, for predicting nonlinear scattering, an iterative method is introduced in the following, which consists of the superposition of a sequence of velocity potential solutions forced by progressively decreasing nonlinear field terms.

As typically done in sound scattering analysis, let us introduce an incident velocity potential field, φ^I, associated with the propagating impinging wave, which is assumed to be independent of the body and governed by the equation

$$-\Box^2\varphi^I = \sigma^{\mathrm{EXT}} = \sum_i S_i^I(t)\,\delta(\mathbf{x} - \mathbf{x}_i) \tag{8}$$

with the forcing terms consisting of a suitable combination of "frozen sources" of time-variant intensities, $S_i^I(t)$, located at $\mathbf{x}_i$.

Then, the total velocity potential is defined as the superposition of the incident velocity potential with the perturbation field generated by the presence of the body. In turn, this is given by the superposition of the velocity potential perturbation generated by the motion of the body (radiated velocity potential), φ^0, such that

$$-\Box^2\varphi^0 = \sigma(\varphi^0) \tag{9}$$

and the scattered potential, φ^S, such that

$$-\Box^2\varphi^S = \sigma(\varphi) - \sigma(\varphi^0) \tag{10}$$

where $\varphi = \varphi^0 + \varphi^S + \varphi^I$.

Previous research has demonstrated that the flow-field generated by the body motion may significantly affect the scattered field, and that its effects are taken into account by the fluid nonlinearities appearing in Eq. (10) [13,14,23–26]. Thus, the nonlinear scattering problem is solved by iteratively superposing incremental contributions of φ^S.

First, the radiated velocity potential, φ^0, is solved through application of the boundary integral formulation in Eq. (7) with the boundary condition

$$\eta = \eta^0 = \frac{\partial \varphi^0}{\partial n} = \mathbf{v}_\xi \cdot \mathbf{n}$$

and the corresponding field term

$$\sigma = \sigma^0 = \sigma(\varphi^0)$$

Next the scattered velocity potential field induced by the incident field is decomposed into several sub-components, namely

$$\varphi^S = \sum_{j=1}^{N_S} \varphi^{S,j} \tag{11}$$

such that

$$|\varphi^{S,1}| > |\varphi^{S,2}| > |\varphi^{S,3}| > \dots$$

and with N_S denoting the order of the component still providing non-negligible contribution.

It is assumed that $\varphi^{S,1}$ is obtained from the formulation in Eq. (7) with the boundary condition

$$\eta = \eta^1 = \frac{\partial \varphi^{S,1}}{\partial n} = -\frac{\partial \varphi^I}{\partial n}$$

and the nonlinear term given by the incremental contribution due to φ^I given by

$$\sigma = \sigma^1 = \sigma(\varphi^0 + \varphi^I) - \sigma(\varphi^0) \tag{12}$$

Therefore $\varphi^{S,1}$ represents the component of the scattered field forced by the incident wave both through the impermeability boundary conditions (the dominating term) and the nonlinear field terms due to φ^0 and φ^I. The contribution of $\varphi^{S,1}$ to σ^1 is omitted so as to have known field terms.

However, once $\varphi^{S,1}$ is evaluated, its incremental contribution to σ yields the second element of the scattered potential series, $\varphi^{S,2}$. Specifically, $\varphi^{S,2}$ is obtained as solution of Eq. (7) with the boundary condition

$$\eta = \eta^2 = \frac{\partial \varphi^{S,2}}{\partial n} = 0$$

(note that the impermeability condition is satisfied by the combination of φ^0 and $\varphi^{S,1}$) and the nonlinear term as given by the incremental contribution

$$\sigma = \sigma^2 = \sigma(\varphi^0 + \varphi^I + \varphi^{S,1}) - \sigma(\varphi^0 + \varphi^I) \tag{13}$$

Therefore $\varphi^{S,2}$ represents the first correction to the scattered potential due to scattered potential nonlinearities (note that, the comparison between Eqs. (12) and (13) shows that the sum of the first and second scattered components, $\varphi^{S,1} + \varphi^{S,2}$, obtained from Eq. (7) satisfies Eq. (10) with the first term on the right-hand side depending only to the first scattered component, $\varphi^{S,1}$).

This procedure is repeated until the $j-$th incremental correction of the scattered velocity potential, $\varphi^{S,j}$, obtained as solution of Eq. (7) with the homogeneous boundary condition

$$\eta = \eta^j = \frac{\partial \varphi^{S,j}}{\partial n} = 0$$

and

$$\sigma = \sigma^j = \sigma(\varphi^0 + \varphi^I + \varphi^{S,1} + \dots + \varphi^{S,j-1}) - \sigma(\varphi^0 + \varphi^I + \varphi^{S,1} + \dots + \varphi^{S,j-2}) \tag{14}$$

becomes negligible for $j = N_S$. It is worth noting that summing the progressively decreasing forcing terms, σ^j, over all cascade steps yields a telescoping series where all intermediate terms cancel out. As a result, the superposition of the equations governing all the incremental components, $\varphi^{S,j}$, perfectly reconstructs Eq. (9), recovering exactly the total nonlinear forcing term, $\sigma(\varphi) - \sigma(\varphi^0)$, on its right-hand side.

The sum of all the N_S components of the scattered field obtained from the application of Eq. (7) satisfies Eq. (10), with the first term on the right-hand side of that equation coinciding with the first term on the right-hand side of Eq. (14) for $j = N_S$.

Finally, it is worth noting that the cascade methodology described above can also be applied to determine the radiated potential, φ^0, as the solution of the nonlinear problem in Eq. (9). This is achieved by removing the incident-field contribution, replacing the scattered-potential subcomponents with the corresponding radiated-field components, and taking the first component as the solution of the associated linear problem subject to impermeability boundary conditions.

3. Velocity potential cascade BEM solution through harmonic balance

For the purpose of the numerical application of the above boundary integral formulation, the surface of the body is discretized into N_p quadrilateral panels, while N_v volume elements are used to discretize the fluid domain where the field integral is evaluated.

In these surface panels and volume elements the velocity potential and its space and time derivatives are assumed to be uniformly distributed, equal to those evaluated at their centroids (zeroth-order Boundary Element Method, BEM).

When the formulation in Eq. (7) is applied as a boundary integral equation with unknown velocity potential over the body surface and known field contributions (as for the solutions of the scattered potential cascade), the satisfaction of the equation is imposed at the center of each surface discretization panel (collocation method). This yields the following set of algebraic equations whose solution provides the piecewise constant values of the velocity potential over the surfaces of the panels

$$\frac{1}{2}\varphi_k(t_*) = \sum_{m=1}^{N_p} A_{km}\eta_m(t_* - \theta_{km}) + \sum_{m=1}^{N_p} B_{km}\varphi_m(t_* - \theta_{km}) + \sum_{m=1}^{N_p} C_{km}\dot{\varphi}_m(t_* - \theta_{km}) + \sum_{m=1}^{N_p} F_{km}\varphi^t_m(t_* - \theta_{km}) + \sum_{h=1}^{N_v} H_{kh}\sigma_h(t_* - \theta_{kh}) \tag{15}$$

where φ_m, η_m and φ^t_m denote, respectively, velocity potential, the normal derivative of the velocity potential (see Eq. (3)), and derivative of the velocity potential along the direction of the tangential local body Mach number, $\mathbf{M}_t = \mathbf{M} - M_n\mathbf{n}$, evaluated at the center of the mth panel. In addition, θ_{km} represents the signal transmission delay θ related to the observer at the center of the kth panel and the emitting source at the center of the mth panel, while σ_h is the nonlinear forcing term evaluated at the center of the hth volume. The time-varying influence coefficients are defined as

$$A_{km}(t_*) = \iint_{\Omega_m} (1 - M_n^2)\, G_0\, J \Big|_{\theta_{km}} \mathrm{d}\xi^1\mathrm{d}\xi^2$$

$$B_{km}(t_*) = \iint_{\Omega_m} \left[-\frac{\partial G_0}{\partial n}\, J + \frac{1}{\Theta}\frac{\partial}{\partial t}\Big|_{\xi} (G_0\,\Lambda) \right]\Big|_{\theta_{km}} \mathrm{d}\xi^1\mathrm{d}\xi^2$$

$$C_{km}(t_*) = \iint_{\Omega_m} \left[\frac{M_n}{c_0} G_0\, J + G_0 \frac{\Lambda}{\Theta} \right]\Big|_{\theta_{km}} \mathrm{d}\xi^1\mathrm{d}\xi^2$$

$$F_{km}(t_*) = -\iint_{\Omega_m} M_n\, M_t\, G_0\, J \Big|_{\theta_{km}} \mathrm{d}\xi^1\mathrm{d}\xi^2$$

$$H_{kh}(t_*) = \iiint_{\mathcal{V}_{\Omega_h}} G_0\, J \Big|_{\theta_{kh}} \mathrm{d}\xi^1\mathrm{d}\xi^2\mathrm{d}\xi^3$$

where $\Lambda = J\,(-\mathbf{e}_r \cdot \mathbf{n} + M_n)/c_0$, while Ω_m, $\mathcal{V}_{\Omega_h}$ indicate, respectively, the (ξ^1, ξ^2)-domain and the (ξ^1, ξ^2, ξ^3)-domain where the surface of the mth panel and the volume of the hth field element are mapped.

The factor $1/2$ appearing at the left-hand side of Eq. (15) takes into account the contribution of the free terms deriving from the singularity of the kernel function $\partial G_0/\partial n$ arising when the position of the observer tends to the limit on the emitting surface (as happens in a boundary integral equation problem such as the present one). Thus, when $k = m$ the coefficients B_{km} are intended as Cauchy principal values of the surface integral (namely, integrals taken symmetrically around the singularity) [27].

Once the velocity potential over the body surface is known, it may be readily used to determine the velocity potential field radiated at external points and, in particular, to evaluate the velocity potential at the centroids of the discretization volumes for the definition of the forcing field terms in the cascade solution process. This is obtained through application of the discretized boundary integral representation. Indeed, in this case, the observers are far from the scattering surface, no singularities occur and, thus, the boundary integral solution is formally identical to Eq. (15) with the factor $1/2$ at the left-hand side replaced by 1 (all surface integrals are regular) [27].

3.1. Multi-harmonic solution algorithm

The integral formulation in Eq. (7) is expressed in the time domain. However, acoustic scattering problems are generally represented in the frequency domain because acoustic scattering phenomena typically deal with high-frequency signals, for which time-domain solution algorithms are subject to the occurrence of numerical instabilities that prevent the evaluation of accurate and reliable solutions (see, for instance, Ref. [21]).

Considering an arbitrarily deforming scatterer in arbitrary motion, the above coefficients of the BEM formulation turn out to be time-varying. To determine a frequency-domain expression of the scattered field, let us assume that the incident velocity potential is harmonic with frequency ω_I, and that the influence coefficients are periodic, with their fundamental harmonic (whose frequency coincides with that of the scatterer deformation, ω_d) being a multiple or a sub-multiple of the harmonic of the incident signal. Note that this assumption is not too limiting nor unrealistic. It is applicable, for example, in all those cases where the deformation of the scatterer is the result of the response of an elastic structure to an incident harmonic pressure wave.

Thus, following the approach applied in Refs. [21] and [28], it is convenient to express the velocity potential at each centroid of the discretized BEM domain in terms of its Fourier series as

$$\varphi_m(t_* - \theta) = \varphi_{m0} + \sum_{n=1}^{N_a} \varphi^c_{mn} \cos\left[n\omega(t_* - \theta)\right] + \sum_{n=1}^{N_a} \varphi^s_{mn} \sin\left[n\omega(t_* - \theta)\right] \tag{16}$$

with ω representing the frequency of the fundamental harmonic, such that $\omega = \min[\omega_d, \omega_I]$. In this equation N_a is the number of harmonics included in the analysis, φ^c_{mn} and φ^s_{mn} are the cosine and sine components of the nth harmonic of the velocity potential at the center of the mth panel, while φ_{m0} denotes its time-average value.

The application of Eq. (16) to express the velocity potential in Eq. (15) yields

$$\varphi_k(t_*) = \sum_{m=1}^{N_p} \hat{B}_{km}(t_*)\,\varphi_{m0} + \sum_{n=1}^{N_a}\sum_{m=1}^{N_p} D^{nc}_{km}(t_*)\,\varphi^c_{mn} + \sum_{n=1}^{N_a}\sum_{m=1}^{N_p} D^{ns}_{km}(t_*)\,\varphi^s_{mn} + f^{\eta}_k(t_*) + f^{\sigma}_k(t_*) \tag{17}$$

with the time-varying coefficients given by

$$D^{nc}_{km}(t_*) = \left[\frac{1}{2}\,\delta_{km} + B_{km}(t_*) + \sum_{j=1}^{N_p} F_{kj}(t_*)\,G_{jm}(t_*)\right]\cos\left[n\omega(t_* - \theta_{km})\right] - n\omega\,C_{km}(t_*)\sin\left[n\omega(t_* - \theta_{km})\right] \tag{18}$$

$$D^{ns}_{km}(t_*) = \left[\frac{1}{2}\,\delta_{km} + B_{km}(t_*) + \sum_{j=1}^{N_p} F_{kj}(t_*)\,G_{jm}(t_*)\right]\sin\left[n\omega(t_* - \theta_{km})\right] + n\omega\,C_{km}(t_*)\cos\left[n\omega(t_* - \theta_{km})\right] \tag{19}$$

$$\hat{B}_{km}(t_*) = \frac{1}{2}\,\delta_{km} + B_{km}(t_*) + \sum_{j=1}^{N_p} F_{kj}(t_*)\,G_{jm}(t_*) \tag{20}$$

where $G_{jm}(t_*)$ are the coefficients providing φ^i at the center of the jth panel from the knowledge of the velocity potentials φ_m, for $m = 1, \dots, N_p$. In addition, the forcing terms derived from the Neumann boundary condition are expressed as

$$f^{\eta}_k(t_*) = \sum_{m=1}^{N_p} A_{km}(t_*)\,\eta_m(t_* - \theta_{km})$$

while those derived from the nonlinear field contributions are given by

$$f^{\sigma}_k(t_*) = \sum_{h=1}^{N_v} H_{kh}(t_*)\,\sigma_h(t_* - \theta_{kh}) \tag{21}$$

Next, determining the Fourier series expansion of the coefficients $\hat{B}_{km}$, D^{nc}_{km}, D^{ns}_{km} and of the forcing terms f^{η}_k, f^{σ}_k, and balancing the left-hand-side and right-hand-side harmonics in Eq. (17) provides the following form of the solution (see Refs. [21] and [28] for details)

$$\boldsymbol{\varphi} = (\mathbf{I} - \mathbf{D})^{-1}\mathbf{f} \tag{22}$$

where

$$\boldsymbol{\varphi} = \begin{bmatrix} \boldsymbol{\varphi}_0 \\ \boldsymbol{\varphi}_{1c} \\ \boldsymbol{\varphi}_{1s} \\ \vdots \\ \boldsymbol{\varphi}_{N_a c} \\ \boldsymbol{\varphi}_{N_a s} \end{bmatrix}, \quad \mathbf{f} = \begin{bmatrix} \mathbf{f}^{\eta}_0 + \mathbf{f}^{\sigma}_0 \\ \mathbf{f}^{\eta}_{1c} + \mathbf{f}^{\sigma}_{1c} \\ \mathbf{f}^{\eta}_{1s} + \mathbf{f}^{\sigma}_{1s} \\ \vdots \\ \mathbf{f}^{\eta}_{N_a c} + \mathbf{f}^{\sigma}_{N_a c} \\ \mathbf{f}^{\eta}_{N_a s} + \mathbf{f}^{\sigma}_{N_a s} \end{bmatrix}$$

with $\boldsymbol{\varphi}_{nc}$ and $\boldsymbol{\varphi}_{ns}$ denoting, respectively, the vector collecting the nth cosine and sine components of the velocity potentials at the N_p body surface centroids. Moreover, $\mathbf{f}^{\eta}_{nc}, \mathbf{f}^{\sigma}_{nc}$ and $\mathbf{f}^{\eta}_{ns}, \mathbf{f}^{\sigma}_{ns}$ indicate the vectors collecting the nth cosine and sine components of the forcing terms, respectively. The matrix $\mathbf{D}$ is a square matrix of dimensions $N_p(2N_a + 1) \times N_p(2N_a + 1)$

$$\mathbf{D} = \begin{bmatrix} \hat{\mathbf{B}}_0 & \mathbf{D}^{1c}_0 & \mathbf{D}^{1s}_0 & \dots & \mathbf{D}^{N_a c}_0 & \mathbf{D}^{N_a s}_0 \\ \hat{\mathbf{B}}_{1c} & \mathbf{D}^{1c}_{1c} & \mathbf{D}^{1s}_{1c} & \dots & \mathbf{D}^{N_a c}_{1c} & \mathbf{D}^{N_a s}_{1c} \\ \hat{\mathbf{B}}_{1s} & \mathbf{D}^{1c}_{1s} & \mathbf{D}^{1s}_{1s} & \dots & \mathbf{D}^{N_a c}_{1s} & \mathbf{D}^{N_a s}_{1s} \\ \vdots & \vdots & \vdots & \ddots & \vdots & \vdots \\ \hat{\mathbf{B}}_{N_a c} & \mathbf{D}^{1c}_{N_a c} & \mathbf{D}^{1s}_{N_a c} & \dots & \mathbf{D}^{N_a c}_{N_a c} & \mathbf{D}^{N_a s}_{N_a c} \\ \hat{\mathbf{B}}_{N_a s} & \mathbf{D}^{1c}_{N_a s} & \mathbf{D}^{1s}_{N_a s} & \dots & \mathbf{D}^{N_a c}_{N_a s} & \mathbf{D}^{N_a s}_{N_a s} \end{bmatrix} \tag{23}$$

obtained by assembling sub-matrices, each of which collects a specific component of the Fourier-series expansion similar to that in Eq. (16) of the time-varying coefficients in Eqs. (18)–(20), and has dimensions $N_p \times N_p$. For instance, the matrices $\mathbf{D}^{1c}_{1c}$ and $\mathbf{D}^{1c}_{1s}$ collect, respectively, the first cosine and sine components of the coefficients $D^{1c}_{km}(t_*)$ expressed by Eq. (18), while $\hat{\mathbf{B}}_{1s}$ collects the first sine components of the coefficients $\hat{B}_{km}(t_*)$ expressed by Eq. (20), for $k, m = 1, \dots, N_p$.

As mentioned above, once the values of the scattered potential over the body's panels are obtained, it is necessary to determine the scattered potential in the field in order to evaluate the contributions σ^j and hence the forcing terms f^{σ}_k (see Eqs. (14) and (21)). It may be readily determined through the proposed numerical algorithm applied to the integral formulation conceived as an integral

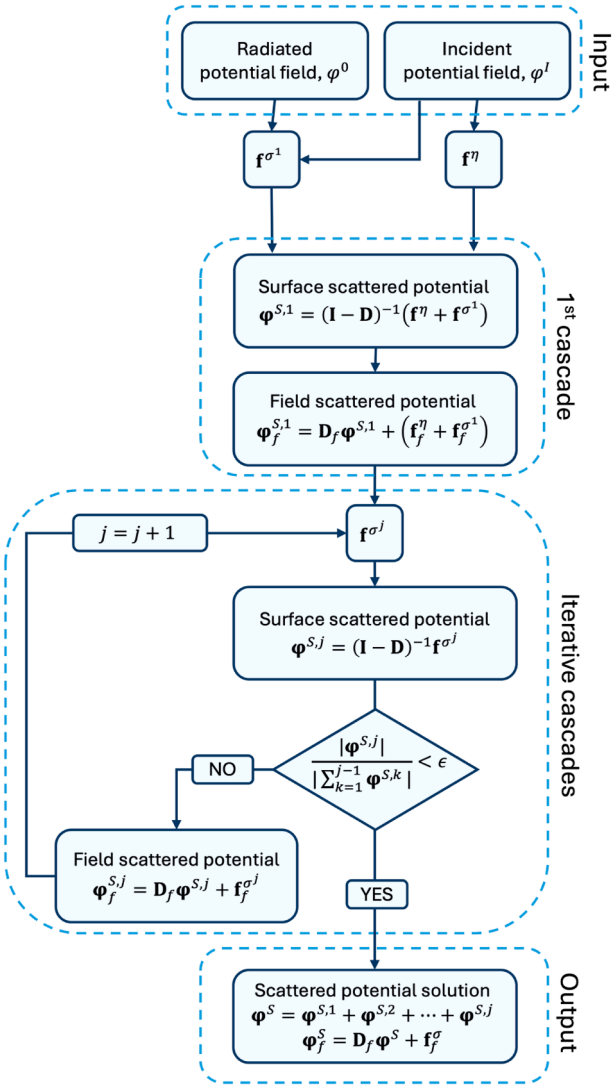

Fig. 1. Flowchart of the proposed numerical procedure for nonlinear sound scattering analysis.

representation. In this case, the integral solution can be formally expressed through Eq. (17) applied at the N_v centroids of the volume elements surrounding the scatterer, with the free term contributions $1/2\delta_{km}$ in the coefficients in Eqs. (18)–(20) removed (no singular integrals appear). Indeed, for $\boldsymbol{\varphi}_f$ denoting the vector of dimensions $N_v(2N_a + 1)$ which collects the Fourier coefficients of the scattered pressure at these points we have

$$\boldsymbol{\varphi}_f = \mathbf{D}_f \, \boldsymbol{\varphi} + \mathbf{f}_f \tag{24}$$

where $\mathbf{D}_f$ is the rectangular matrix of dimensions $N_v(2N_a + 1) \times N_p(2N_a + 1)$ (similar to matrix $\mathbf{D}$ in Eq. (23)) that collects the Fourier components of the BEM coefficients for external observers, while $\mathbf{f}_f$ collects the Fourier components of the forcing terms evaluated for the same observers.

Fig. 1 shows a flowchart summarizing the proposed numerical procedure for the determination of nonlinear sound scattering from deforming bodies, where ϵ represents the limit of convergence of the iterative process.

It is worth highlighting that the results presented in [21] correspond to the first scattering component, $\varphi^{S,1}$, under the assumption of neglecting the effects of the fluid nonlinearities.

Finally, note that the proposed solution procedure can be applied to an arbitrarily deforming scatterer. Indeed, if ω_d and ω_I are arbitrary, the set of harmonics of the scattered sound is given by $\omega_k = \omega_I \pm k\omega_d$. In this case, the fundamental harmonic, ω, and the number of harmonics, N_a, of the Fourier series introduced in Eq. (3.1) must be chosen so as to adequately capture the harmonics, ω_k, appearing in the resulting scattered signal (indeed, in this case, the proposed frequency solution process can be considered equivalent to the application of discrete Fourier transforms).

Table 1
Numerical convergence on discretization mesh and computational effort.

Mesh	$\epsilon_r^2\|_{n=1}$	$\epsilon_r^2\|_{n=2}$	$\epsilon_r^2\|_{n=3}$	Time	RAM
$12\times6\times6$	0.08%	4.53%	3.33%	0h 41m	78.4 MB
$16\times8\times7$	0.02%	2.85%	1.82%	5h 38m	302 MB
$20\times10\times8$	0.007%	0.85%	0.53%	30h 22m	881 MB
$24\times12\times9$	–	–	–	124h 20m	2.15 GB

4. Numerical results

The objective of this paper is to present a novel theoretical-numerical formulation for the analysis of sound scattering by moving and deforming bodies, accounting for fluid nonlinearities. Accordingly, and without loss of generality, the capabilities of the proposed approach are assessed through a numerical investigation of the canonical problem of a pulsating sphere subjected to an incident plane wave, for which an analytical solution for linear sound scattering is available [15,21].

For simplicity, and to focus on nonlinear scattering effects, the cases considered in the following concern pulsating spheres with a maximum surface Mach number equal to 0.06, and nonlinearities associated with the radiated field, $\sigma^0 = \sigma(\varphi^0)$, which remain negligible. The maximum Mach number associated with the considered traveling waves is approximately 0.012, so that the flow field is free from shock formation. It is worth noting that, if non-negligible, the nonlinear terms σ^0 would not formally alter the solution procedure for the scattered sound field, but would affect only the computation of the radiated field (see Eq. (9)).

Initially, let us consider a sphere of radius $r_0 = 1$ m subject to pulsations of amplitude $a_d = 0.2r_0$ and frequency, ω_d, such that $k_d r_0 = 0.3$ (with $k_d = \omega_d/c_0$ denoting the deformation wave number), impinged by a plane wave of velocity potential, φ^I, of amplitude A^I and wave number $k_I = k_d$. For this problem and for all pulsating spheres considered in the following, the radiated potential, φ^0, is determined through the method for determining the linear analytical solution presented in [28], while, for simplicity, and without loss of generality, the wave numbers k_d and k_I associated with the sphere pulsation and the incident sound wave, respectively, are assumed to be identical (as explained in Eq. (3.1), the proposed solution algorithm can always be suitably applied to any arbitrarily deforming scatterer impinged by a sound wave).

First, a preliminary numerical convergence study is carried out. In particular, four different discretizations of the sphere surface and the surrounding fluid domain are considered. The external domain is assumed to extend radially up to $0.4\,r_0$ (a preliminary numerical investigation, not reported here for brevity, indicated that beyond this distance the field contributions become negligible), and four harmonics, $N_a = 4$, are retained to represent the time evolution of the signals (this aspect is further discussed later). Convergence is investigated by progressively increasing the number of meridians and parallels used to discretize the sphere surface, as well as the number of radial elements employed in the discretization of the surrounding volume.

After obtaining the solutions corresponding to the converged cascade processes (the convergence rate is discussed later), the relative L2-norm differences, ϵ_r^2, between the first three harmonics of the scattered signal computed using the finest mesh and those obtained with the coarser meshes are evaluated and reported in Table 1. In the table, each mesh is characterized by the number of surface-discretization meridians, N_m, parallel circles N_c, and radial volume elements, N_r, and is denoted as $N_m \times N_c \times N_r$, while $\epsilon_r^2|_n$ represents the relative L2-norm difference regarding the $n-$th harmonic. The relative L2-norm difference for each harmonic is computed by comparing the scattered signal obtained with the finest mesh, $|\varphi_4^S|$, with those obtained using the first three meshes, $|\varphi_j^S|$ $(j = 1, 2, 3)$, and is defined as follows:

$$\epsilon_r^2 = \frac{\sum_{i=1}^{N_o} \left(|\varphi_{j,i}^S| - |\varphi_{4,i}^S| \right)^2}{\sum_{i=1}^{N_o} (|\varphi_{4,i}^S|)^2}$$

where N_o denotes the number of observation points located on a circle at a distance $d = 10\,r_0$ from the sphere center, lying on a plane perpendicular to the plane of the impinging wave with $A^I = 1$ m^2/s.

These results indicate that a relative L2-norm difference below 1% is achieved using a mesh comprising $N_p = 200$ surface panels (20 meridians and 10 parallels) and $N_v = 1600$ volume elements in the surrounding field region. This mesh represents an effective compromise between numerical accuracy and computational cost, as further mesh refinement yields only marginal changes in the predicted results.

Next, with this mesh kept fixed, the scattered field is also evaluated using different numbers of harmonics of the signal, namely, $N_a = 2, 3, 4, 5$. The relative L2-norm differences, ϵ_r^2, between the first three harmonics of the scattered signal computed with $N_a = 5$ and those obtained with $N_a = 2, 3, 4$ are evaluated and reported in Table 2 (note that, for $N_a = 2$ the third harmonic of the signal cannot be determined). These results indicate that adopting $N_a = 4$ yields converged predictions for the first three harmonics of the scattered field.

According to the above investigations, all analyses and results presented in the following, including cases characterized by lower and less critical surface Mach numbers, are obtained using $N_p = 200$, $N_v = 1600$, and $N_a = 4$.

Table 2
Numerical convergence on number of signal harmonics.

N_a	$\epsilon_r^2\|_{n=1}$	$\epsilon_r^2\|_{n=2}$	$\epsilon_r^2\|_{n=3}$
2	$1 \cdot 10^{-2}$%	$5 \cdot 10^{-1}$%	–
3	$3 \cdot 10^{-5}$%	$8 \cdot 10^{-4}$%	$4 \cdot 10^{-2}$%
4	$6 \cdot 10^{-6}$%	$4 \cdot 10^{-4}$%	$2 \cdot 10^{-3}$%

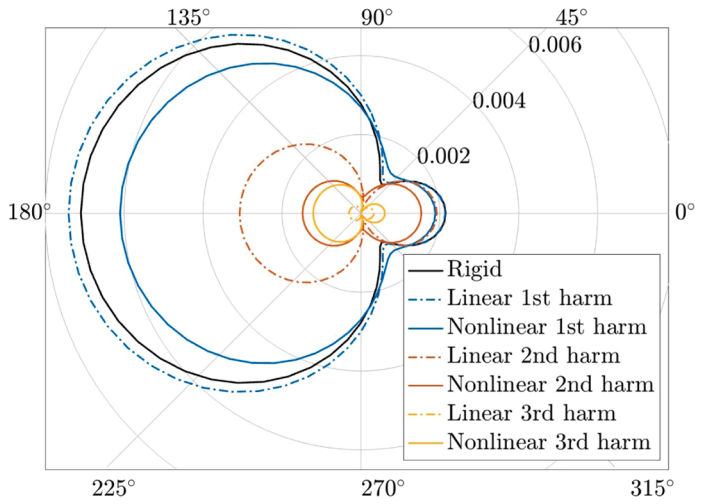

Fig. 2. Multi-harmonic directivity patterns of the scattered signal provided by linear and nonlinear solutions. $a_d = 0.2r_0$, $k_d r_0 = 0.3$, $A^I = 1$ m^2/s, $d/r_0 = 10$. Radial values denote $|\varphi^S|/|\varphi^I|$.

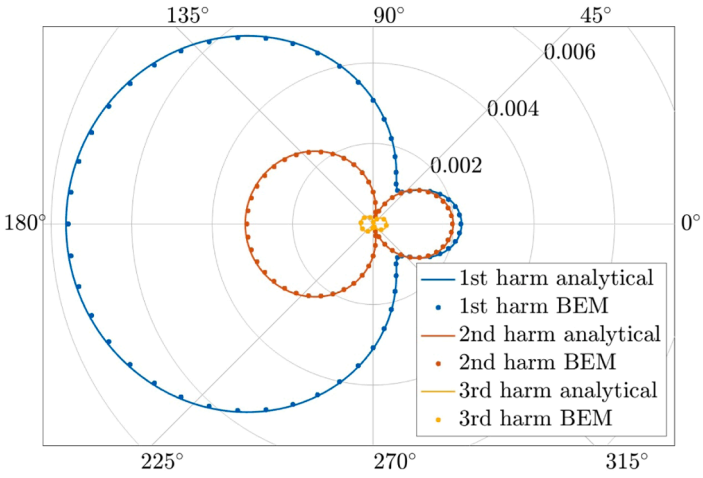

Fig. 3. Directivity pattern of scattered signal provided by linear BEM prediction and analytical solution. $a_d = 0.2r_0$, $k_d r_0 = 0.3$, $A^I = 1$ m^2/s, $d/r_0 = 10$. Radial values denote $|\varphi^S|/|\varphi^I|$.

For completeness, note that Table 1 also reports the computational resources required by each discretization mesh, in terms of both memory usage and runtime. All numerical experiments were performed on a standard Linux desktop workstation equipped with an Intel Core i9-14900 processor (24 cores, up to 5.8 GHz) and 192 GB of RAM.

Fig. 2 presents the directivity patterns of the first three harmonics of the scattered signal. In particular, it compares the results obtained by the linear formulation introduced in [21] (equivalent to the first contribution to the present cascade solution, $\varphi^{S,1}$, when the nonlinear effects of φ^0 and φ^I are negligible), with the proposed nonlinear solution which includes the distortion effects due to the flow generated by pulsations (represented by field terms involving φ^0, φ^I and φ^S). In addition, the mono-harmonic solution for the rigid sphere is depicted. This figure proves that, as expected, the scattered signal is multi-harmonic (both due to pulsating boundary conditions and fluid nonlinearities), and that the fluid flow generated by sphere pulsations may produce significant distortion to all harmonics of the scattered signal, and thus its contribution cannot be neglected (a dedicated numerical investigation proved that nonlinear terms not involving φ^0 provide negligible contributions).

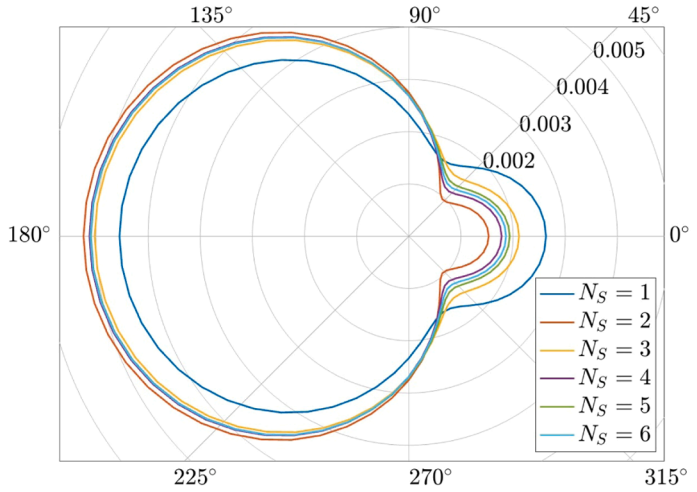

Fig. 4. Incremental effect of cascade components on the directivity patterns of the first harmonic of the scattered signal. $a_d = 0.2r_0$, $k_d r_0 = 0.3$, $A^I = 1$ m^2/s, $d/r_0 = 10$. Radial values denote $|\varphi^S|/|\varphi^I|$.

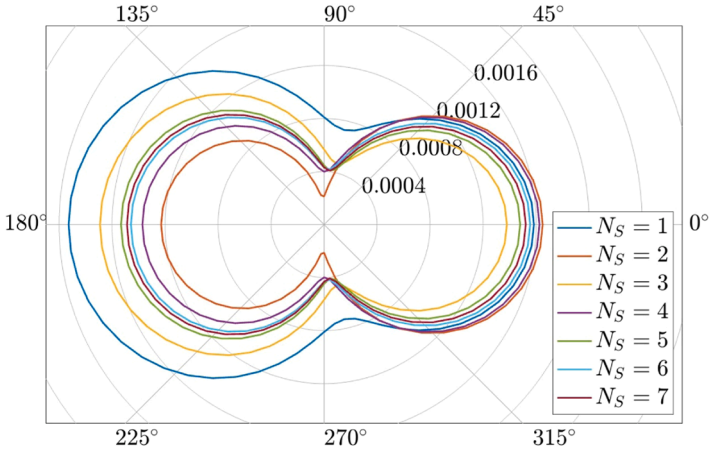

Fig. 5. Incremental effect of cascade components on the directivity patterns of the second harmonic of the scattered signal. $a_d = 0.2r_0$, $k_d r_0 = 0.3$, $A^I = 1$ m^2/s, $d/r_0 = 10$. Radial values denote $|\varphi^S|/|\varphi^I|$.

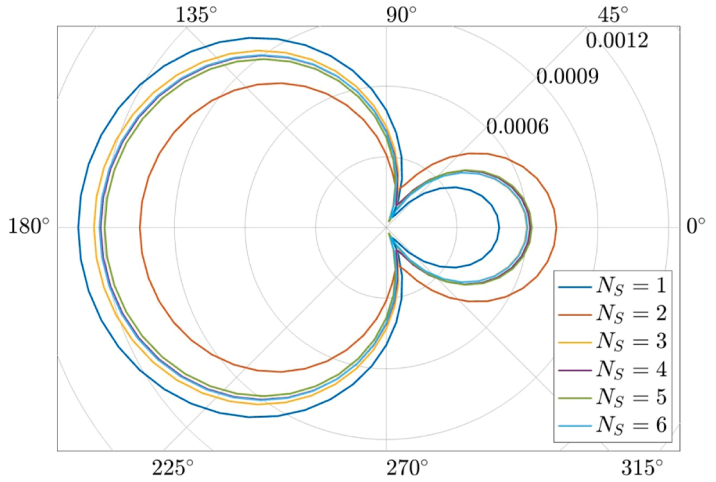

Fig. 6. Incremental effect of cascade components on the directivity patterns of the third harmonic of the scattered signal. $a_d = 0.2r_0$, $k_d r_0 = 0.3$, $A^I = 1$ m^2/s, $d/r_0 = 10$. Radial values denote $|\varphi^S|/|\varphi^I|$.

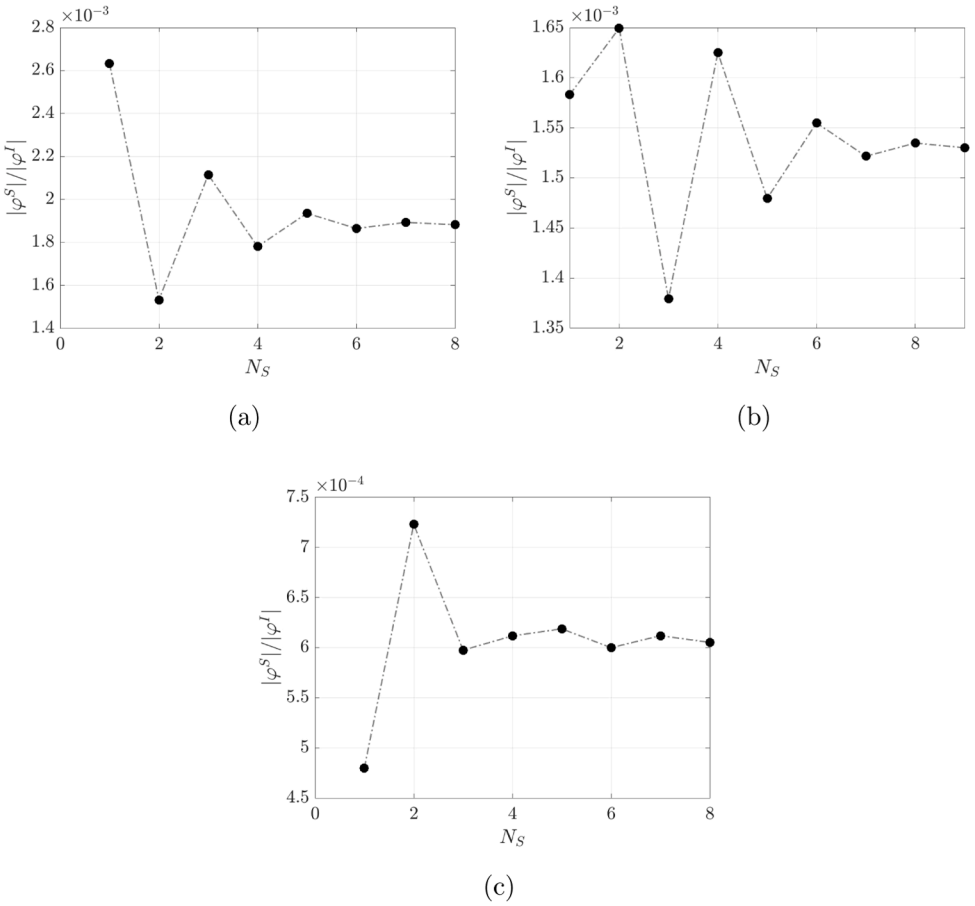

Fig. 7. Scattered potential at the observer point located at the azimuth position $\psi = 0°$. (a): first harmonic; (b): second harmonic; (c): third harmonic.

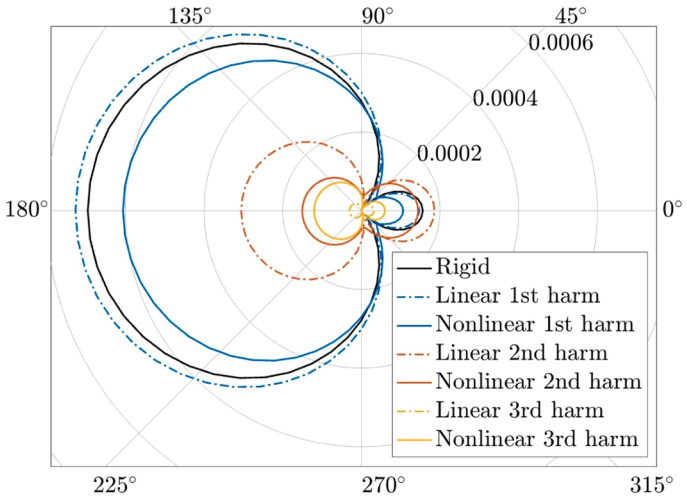

Fig. 8. Multi-harmonic directivity patterns of the scattered signal provided by linear and nonlinear solutions. $a_d = 0.2r_0$, $k_a r_0 = 0.3$, $A^I = 1$ m^2/s, $d/r_0 = 100$. Radial values denote $|\varphi^S|/|\varphi^I|$.

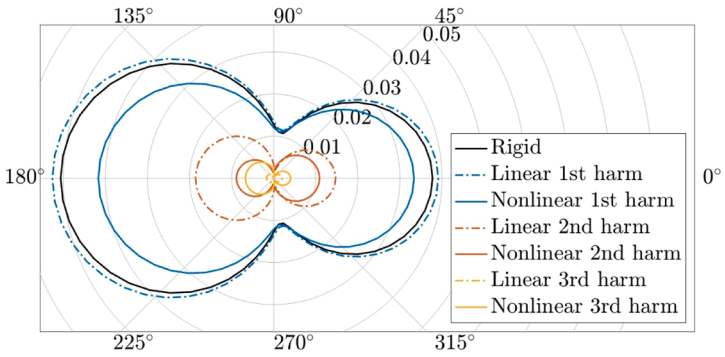

Fig. 9. Multi-harmonic directivity patterns of the scattered signal provided by linear and nonlinear solutions. $a_d = 0.2r_0$, $k_d r_0 = 0.3$, $A^I = 1$ m^2/s, $d/r_0 = 2$. Radial values denote $|\varphi^S|/|\varphi^I|$.

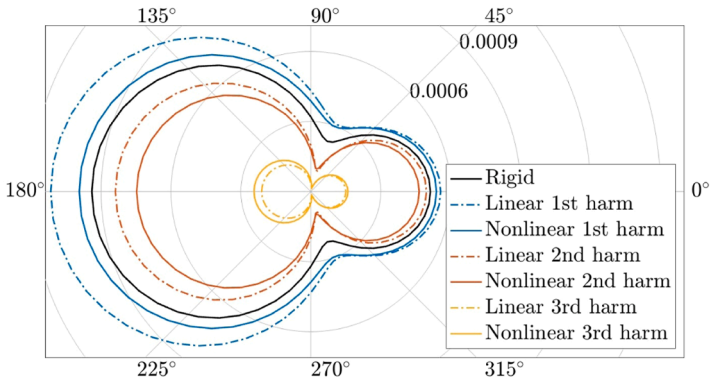

Fig. 10. Multi-harmonic directivity patterns of the scattered signal provided by linear and nonlinear solutions. $a_d = 0.4r_0$, $k_d r_0 = 0.1$, $A^I = 1$ m^2/s, $d/r_0 = 10$. Radial values denote $|\varphi^S|/|\varphi^I|$.

Note that, the linear BEM solver has been extensively validated in [21] against the analytical solution presented in that paper as an extension of the analytical scattering formulation introduced by Censor [15]. As an example, Fig. 3 shows the excellent agreement between the predictions obtained by the linear BEM solver and the analytical solution for the first three harmonics of the scattered signal related to the problem considered in Fig. 2. The nonlinear BEM solver presented here is a straightforward extension of the linear one, and, to the authors' knowledge, neither analytical solutions, numerical simulations, nor experimental data are available in the literature for its validation.

Next, Figs. 4–6 show the incremental effect of the cascade components on the directivity patterns of the first three harmonics of the scattered signal given by the nonlinear BEM solver. They demonstrate the quite rapid decrease in the contributions of the cascade components with increasing iterations, and hence the fast convergence rate of the applied algorithm for the nonlinear solution. For the examined problem, $N_S = 7$ is sufficient to obtain solutions with 2% converged tolerance (see Eq. (11)). This is highlighted in Fig. 7 which depicts, as a function of N_S, the values of the first three harmonics of the scattered potential computed at the surface point first impinged by the incident wave (note that in Figs. 4 and 6 the curve corresponding to $N_S = 7$ is not depicted since graphically coincident with that related to $N_S = 6$).

The comparisons among the different solutions of the scattered field considered in Fig. 2 are repeated for far-field and near-field observers located on a plane perpendicular to the plane of the impinging wave, still assuming $A^I = 1$ m^2/s. These are shown, respectively, in Fig. 8 that presents the multi-harmonic directivity patterns of the scattered signal evaluated at a distance $d = 100\, r_0$ from the sphere centre, and in Fig. 9 where the results regard observers much closer to the sphere centre, placed at $d = 2\, r_0$.

While it is observed that, as expected, different far-field and near-field directivity patterns of scattered signal are obtained, in both cases it is confirmed that all harmonics of the scattered signal are significantly affected by the nonlinear terms associated with the fluid flow generated by the pulsations of the sphere.

Next, a case with lower pulsation frequency and larger pulsation amplitude, and a case with higher pulsation frequency and smaller pulsation amplitude are examined, with the incident planar wave still having $A^I = 1$ m^2/s. In particular, Fig. 10 presents the scattered field at $d/r_0 = 10$, for $a_d = 0.4r_0$ and $k_d r_0 = 0.1$, while, for the same positions of observers, Fig. 11 shows the scattered field for $a_d = 0.1r_0$ and $k_d r_0 = 0.4$.

In both cases the amplitude of the oscillating Mach number of the sphere surface is equal to $k_d a_d = 0.04$, which is smaller than that related to the results in Fig. 2 ($k_d a_d = 0.06$ in that case). For this reason, linear and nonlinear predictions of the scattered signal in

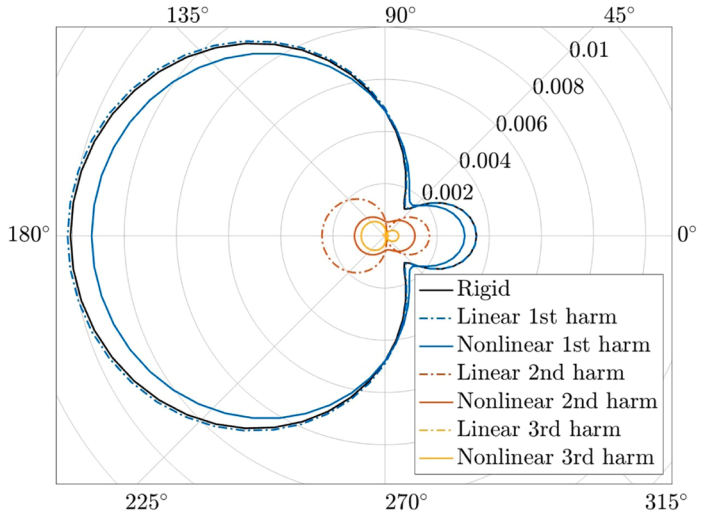

Fig. 11. Multi-harmonic directivity patterns of the scattered signal provided by linear and nonlinear solutions. $a_d = 0.1r_0$, $k_d r_0 = 0.4$, $A^I = 1$ m^2/s, $d/r_0 = 10$. Radial values denote $|\varphi^S|/|\varphi^I|$.

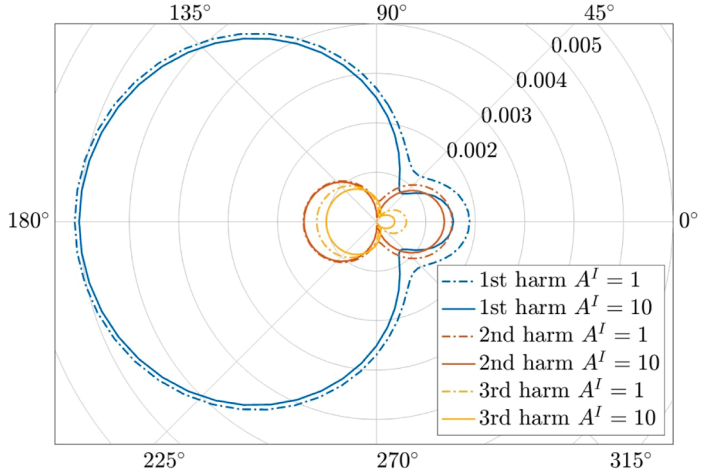

Fig. 12. Multi-harmonic directivity patterns of the scattered signal related to incident waves with $A^I = 1$ m^2/s and $A^I = 10$ m^2/s. $a_d = 0.2r_0$, $k_d r_0 = 0.3$, $d/r_0 = 10$. The unit of measure of the values in the legend is m^2/s. Radial values denote $|\varphi^S|/|\varphi^I|$.

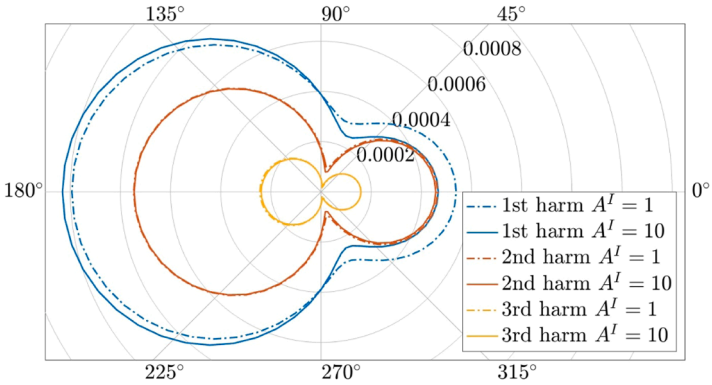

Fig. 13. Multi-harmonic directivity patterns of the scattered signal related to incident waves with $A^I = 1$ m^2/s and $A^I = 10$ m^2/s. $a_d = 0.4r_0$, $k_d r_0 = 0.1$, $d/r_0 = 10$. The unit of measure of the values in the legend is m^2/s. Radial values denote $|\varphi^S|/|\varphi^I|$.

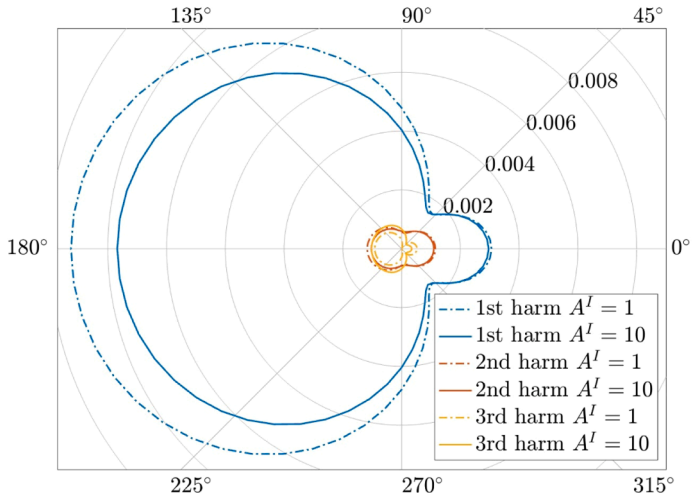

Fig. 14. Multi-harmonic directivity patterns of the scattered signal related to incident waves with $A^I = 1$ m^2/s and $A^I = 10$ m^2/s. $a_d = 0.1r_0$, $k_d r_0 = 0.4$, $d/r_0 = 10$. The unit of measure of the values in the legend is m^2/s. Radial values denote $|\varphi^S|/|\varphi^I|$.

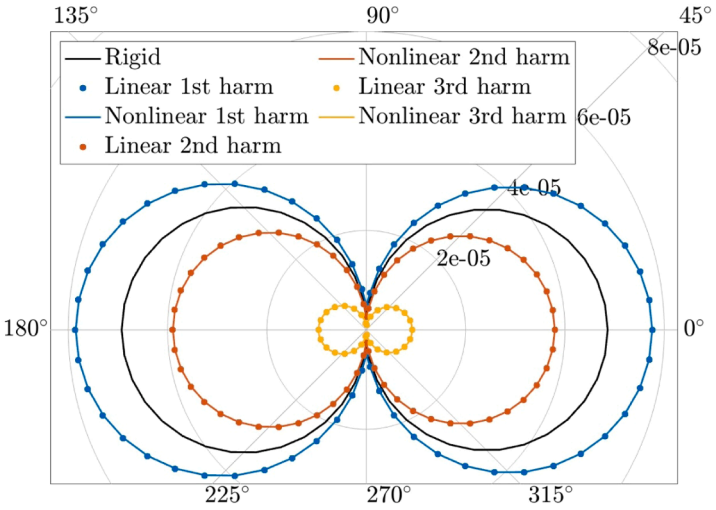

Fig. 15. Multi-harmonic directivity patterns of the scattered signal provided by linear and nonlinear solutions. $a_d = 0.5r_0$, $k_d r_0 = 0.01$, $A^I = 1$ m^2/s, $d/r_0 = 10$. Radial values denote $|\varphi^S|/|\varphi^I|$.

Figs. 10 and 11 are closer than those in Fig. 2. Comparing Figs. 10 and 11 it is interesting to observe that larger-amplitude pulsations produce high harmonics of the scattered signal which are more significant than those arising from the higher-frequency pulsation case (when related to the first harmonic of the signal). This derives from the kinematic nonlinearities produced by the boundary conditions applied over the pulsating sphere. At the same time, however, higher-frequency pulsations generate fluid nonlinearities which significantly affect the higher harmonics of the scattered signal. Indeed, the relative discrepancies between linear and nonlinear predictions of higher harmonics in Fig. 11 are considerably bigger than those observed in the larger-amplitude results of Fig. 10.

When linear scattering analysis is performed, the directivity patterns expressed in terms of the ratio between scattered and incident signal (as typically done and as done in this work) is invariant with respect to the amplitude of the incident signal. This is untrue when nonlinear field terms, σ, are considered. Indeed, as explained in Sect. II, these are given by the combination of terms involving products between φ^0, φ^I and φ^S. As the amplitude of φ^I increases, the corresponding higher-order contributions to σ become significant and the scattered signal is no longer linearly proportional to it. This is shown in Figs. 12–14 for the pulsating sphere cases already examined in Figs. 2, 10 and 11, where the directivity patterns of the scattered velocity potential predicted for $A^I = 1$ m/s^2 and $A^I = 10$ m/s^2 are compared (still expressed in terms of the ratio $|\varphi^S|/|\varphi^I|$). The discrepancies between solid and dashed lines are representative of nonlinear field contributions due to the incident wave. It is interesting to note that when low-frequency/large-amplitude pulsations are considered, the multi-harmonic contributions to the scattered field are dominated by the kinematic nonlinear terms and the effects of increased incident wave amplitude are negligible (see Fig. 13). In this case only the first harmonic is slightly affected by the amplitude of the incident signal. Instead, when higher-frequency pulsations with smaller amplitude are considered, the effects from

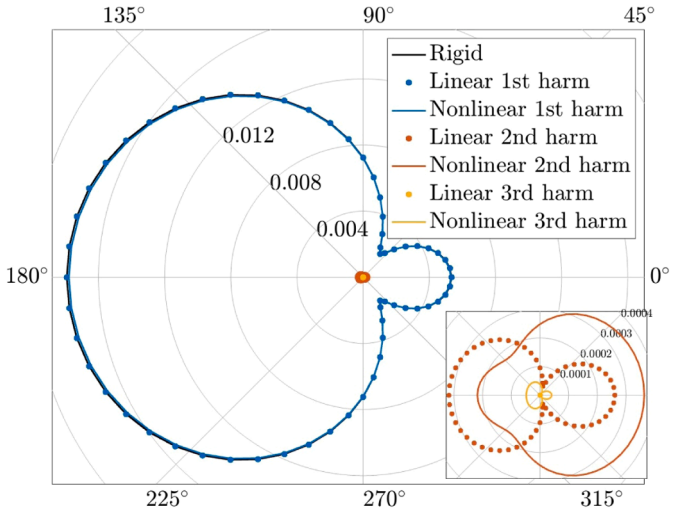

Fig. 16. Multi-harmonic directivity patterns of the scattered signal provided by linear and nonlinear solutions. $a_d = 0.01r_0$, $k_d r_0 = 0.5$, $A^I = 1$ m^2/s, $d/r_0 = 10$. Radial values denote $|\varphi^S|/|\varphi^I|$.

fluid nonlinearities are dominant and the influence of the amplitude of the incident wave is stronger, especially on the directivity pattern of the first harmonic of the scattered signal (see Fig. 14).

Finally, pulsation cases with either large amplitude or high frequency, but very small amplitudes of the surface Mach number are considered. Specifically, the signals scattered by pulsating spheres with $a_d = 0.5r_0, k_d r_0 = 0.01$ and $a_d = 0.01r_0, k_d r_0 = 0.5$, both corresponding to surface Mach number amplitude equal to $k_d a_d = 0.005$, are presented in Figs. 15 and 16, respectively. These results confirm that large amplitude pulsations generate higher harmonics of the scattered signal which are comparable to the first one, and that contributions from fluid nonlinearities are negligible because of the very low surface Mach number and pulsation frequency (in these cases, linear and nonlinear solutions are practically identical, indeed). In addition, it is confirmed also that pulsation frequency affects fluid nonlinearities. This is highlighted by the zoom of higher harmonics in Fig. 16 which are very small due to the very small pulsation amplitude, but present significant discrepancy between linear and nonlinear predictions.

5. Concluding remarks

A novel velocity-potential cascade BEM solution based on a harmonic-balance technique has been introduced to study nonlinear sound scattering of deforming bodies. It takes into account both the kinematic and the fluid nonlinearities produced by the dynamic deformation of the scatterer. The fluid nonlinearities are strongly related to the flow-field around the scatterer and, to the authors' knowledge, the effect on sound scattering of fluid nonlinearities due to body deformation has been examined here for the first time. To focus on nonlinear scattering effects, the numerical investigation considers pulsating spheres impinged by a plane acoustic wave under conditions for which the nonlinear terms associated solely with the radiated sound are negligible. It is worth noting, however, that the proposed solution method remains applicable even when this assumption does not hold. The outcomes have proven that: (i) the proposed harmonic-balance cascade prediction algorithm is capable of providing convergent nonlinear scattered solution in a few iterations (for the cases examined, no more than seven iterations are necessary to obtain converged results); (ii) for a mono-chromatic incident wave, both kinematic and fluid nonlinearities produce a multi-harmonic scattered signal, and this occurs both for near-field and far-field observers; (iii) for a given surface Mach number, the influence of kinematic nonlinearities on the scattered signal increases with the pulsation amplitude, whereas the impact of fluid nonlinearities grows with the pulsation frequency (in other words, kinematic nonlinearities are more strongly associated with the pulsation amplitude than with frequency, while fluid nonlinearities exhibit the opposite behavior); (iv) the amplitudes of the higher harmonics of the scattered signal are strongly related to kinematic nonlinearities; (v) as the amplitude of the incident wave increases, so does its contribution to the fluid nonlinearities, thus appreciably affecting the directivity pattern of the scattered signal. These outcomes demonstrate that accurate analyses of sound scattered by bodies undergoing significant dynamic deformations might require the application of a nonlinear solution approach like that proposed in the present work. It is also necessary when the amplitude of the incident signal is not small, regardless of the deformation of the scatterer. To demonstrate the capabilities of the proposed methodology to analyze nonlinear sound scattering from deforming bodies, the presented study focused on a fundamental case consisting of a pulsating sphere subjected to an incident acoustic wave. However, in the context of potential applications to more industrially relevant configurations, some critical issues may arise. In particular, a large number of panels, volume elements and harmonics could be very demanding in terms of available computational memory. In addition, multi-chromatic incident waves might require the evaluation of a large number of harmonic responses. This implies the need for adequate computational resources and optimized programming (by introducing, for instance, hierarchical BEM

algorithms). Scatterer deformations for which the nonlinear terms associated with the radiated sound are non-negligible will be addressed in future studies.

CRediT authorship contribution statement

B. De Rubeis: Writing – review & editing, Validation, Software, Methodology, Investigation, Conceptualization; **M. Gennaretti:** Writing – review & editing, Writing – original draft, Supervision, Methodology, Conceptualization; **C. Poggi:** Writing – review & editing, Supervision, Software; **G. Bernardini:** Writing – review & editing, Supervision, Software.

Declaration of competing interest

The authors declare that they have no known competing financial interests or personal relationships that could have appeared to influence the work reported in this paper.

Data availability

No data was used for the research described in the article.

References

[1] S.A. Rizzi, D.L. Huff, D.D. Boyd, P. Bent, B.S. Henderson, K.A. Pascioni, D.C. Sargent, D.L. Josephson, M. Marsan, H. He, R. Snider, Urban air mobility noise: current practice, gaps, and recommendations, Nasa TP 2020—5007433 (2020).
[2] International Civil Aviation Organization, Environmental report 2016: On Board a Sustainable Future, Technical Report, ICAO, Montreal, Canada, 2016. https://www.icao.int/environmental-protection/Documents/ICAO%20Environmental%20Report%202016.pdf
[3] E. Commission, Flightpath 2050 - Europe's Vision for Aviation, European Union, 2011.
[4] Q. Ai, M. Azarpeyvand, X. Lachenal, P.M. Weaver, Aerodynamic and aeroacoustic performance of airfoils with morphing structures, Wind Energy 19 (7) (2016) 1325–1339. https://doi.org/10.1002/we.1900
[5] Z. Kan, D. Li, S. Zhao, J. Xiang, E. Sha, Aeroacoustic and aerodynamic characteristics of a morphing airfoil, Aircr. Eng. Aerosp. Technol. 93 (5) (2021) 888–899. https://doi.org/10.1108/AEAT-11-2020-0263
[6] H.A. Schenck, Improved integral formulation for acoustic radiation problems, J. Acoust. Soc. Am. 44 (1) (1968) 41–58. https://doi.org/10.1121/1.1911085
[7] D.G. Crighton, F.G. Leppington, On the scattering of aerodynamic noise, J. Fluid Mech. 46 (3) (1971) 577–597. https://doi.org/10.1017/S0022112071000715
[8] A.F. Seybert, B. Soenarko, Radiation and scattering of acoustic waves from bodies of arbitrary shape in three-dimensional half space, J. Vib. Acoust. 110 (1) (1988) 112–117. https://doi.org/10.1115/1.3269465
[9] G.C. Gaunaurd, Elastic and acoustic resonance wave scattering, Appl. Mech. Rev. 42 (6) (1989) 143–192. https://doi.org/10.1115/1.3152427
[10] D. Colton, R. Kress, Integral Equation Methods in Scattering Theory, Society for Industrial and Applied Mathematics, 2013. https://doi.org/10.1137/1.9781611973167
[11] M.J. Lighthill, On sound generated aerodynamically I. General theory, Proc. R. Soc. A 211 (1107) (1952) 564–587. https://doi.org/10.1098/rspa.1952.0060
[12] J.E. Ffowcs Willams, D.L. Hawkings, Sound generation by turbulence and surfaces in arbitrary motion, Philos. Trans. R. Soc. A 264 (1151) (1969) 321–342. https://doi.org/10.1098/rsta.1969.0031
[13] M. Gennaretti, G. Bernardini, C. Poggi, C. Testa, Velocity-potential boundary-field integral formulation for sound scattered by moving bodies, AIAA J 56 (9) (2018) 3547–3557. https://doi.org/10.2514/1.J056491
[14] C. Testa, C. Poggi, G. Bernardini, M. Gennaretti, Pressure-field permeable-surface integral formulations for sound scattered by moving bodies, J. Sound Vib. 459 (2019) 114860. https://doi.org/10.1016/J.JSV.2019.114860
[15] D. Censor, Scattering by time varying obstacles, J. Sound Vib. 25 (1) (1972) 101–110. https://doi.org/10.1016/0022-460X(72)90599-8
[16] D. Censor, Harmonic and transient scattering from time varying obstacles, J. Sound Vib. 76 (5) (1984) 1527–1534. https://doi.org/10.1121/1.391436
[17] J.C. Piquette, A.L. Van Buren, Nonlinear scattering of acoustic waves by vibrating surfaces, J. Acoust. Soc. Am. 76 (3) (1984) 880–889. https://doi.org/10.1121/1.391313
[18] N. Mujica, R. Wunenburger, S. Fauve, Scattering of a sound wave by a vibrating surface, Eur. Phys. J. B 33 (2003) 209–213. https://doi.org/10.1140/epjb/e2003-00158-7
[19] M. Gennaretti, B. De Rubeis, C. Poggi, G. Bernardini, Deformable-boundary integral formulation for the solution of arbitrarily-forced acoustic wave equation, J. Sound Vib. 591 (2024) 118618. https://doi.org/10.1016/j.jsv.2024.118618
[20] M. Gennaretti, B. De Rubeis, C. Poggi, G. Bernardini, Corrigendum to 'deformable-boundary integral formulation for the solution of arbitrarily-forced acoustic wave equation' [Journal of Sound and Vibration 591 (2024) 118618], J. Sound Vib. 599 (2025) 118921. https://doi.org/10.1016/j.jsv.2024.118921
[21] B. De Rubeis, M. Gennaretti, C. Poggi, G. Bernardini, Sound scattered by deforming bodies through boundary integral formulations, AIAA J 63 (10) (2025) 4196–4209. https://doi.org/10.2514/1.J065258
[22] P.M. Morse, H.B. Feshbach, Methods of Theoretical Physics, McGraw-Hill, NY, 1953.
[23] G. Bernardini, C. Poggi, M. Gennaretti, C. Testa, Study of velocity-potential integral formulations for sound scattered by moving bodies, AIAA J 59 (3) (2021) 1008–1019. https://doi.org/10.2514/1.J059482
[24] K. Taylor, A transformation of the acoustic equation with implications for wind-tunnel and low-speed flight tests, Proc. R. Soc. A 363 (1713) (1978) 271–281. https://doi.org/10.1098/rspa.1978.0168
[25] R.J. Astley, J.G. Bain, A three-dimensional boundary element scheme for acoustic radiation in low mach number flows, J. Sound Vib. 109 (3) (1986) 445–465. https://doi.org/10.1016/S0022-460X(86)80381-9
[26] S. Mancini, R.J. Astley, S. Sinayoko, G. Gabard, M. Tournour, An integral formulation for wave propagation on weakly non-uniform potential flows, J. Sound Vib. 385 (2016) 184–201. https://doi.org/10.1016/j.jsv.2016.08.025
[27] M. Gennaretti, Fundamentals of Aeroelasticity, Springer Nature, Switzerland AG, 2024. https://doi.org/10.1007/978-3-031-53379-2
[28] M. Gennaretti, B. De Rubeis, A boundary integral formulation for predicting acoustic waves generated by large deformations of bodies, Aerosp. Sci. Technol. 164 (2025) 110354. https://doi.org/10.1016/j.ast.2025.110354